Solid Freeform Fabrication 2023: Proceedings of the 34th Annual International Solid Freeform Fabrication Symposium – An Additive Manufacturing Conference
Reviewed Paper

HIGH-PRECISION MEASUREMENT OF MELT POOL PROPERTIES DURING LASER-BASED POWDER BED FUSION OF METALS BY HIGH-SPEED IMAGING

A. Elspaß[a], Jan Wegner[a], Hanna Schönrath[a], Niklas Horstjann[a], S. Kleszczynski[a,b]

[a] Chair of Manufacturing Technology, Institute for Product Engineering, University of Duisburg-Essen, Lotharstraße 1, 47057 Duisburg, Germany
[b] Center for Nanointegration Duisburg- Essen (CENIDE), 47057 Duisburg, Carl-Benz-Str. 199, Germany

Abstract

Laser-based powder bed fusion of metals is used to produce complex and high-performance components for different industrial applications. Due to the high complexity of the underlying physical mechanisms during the process, its control is still challenging. To avoid the formation of defects, which affect mechanical properties, a huge amount of specific know-how is crucial. Especially for regulated industries, such as medical or aerospace, this is a limiting factor for the widespread usage. In this work, high-speed imaging in combination with a high-magnification optic is used to gain deeper insight into the property-determining mechanisms and boundary conditions during the process. Thereby, the intensity distribution from the melt pool radiation is measured and analyzed with an imaging script to determine width, length, and cooling rate with a resolution of 1.44 µm/pixel. The potential of this data for predicting resulting scan track properties is demonstrated. It can be shown that an automatic width measurement deviates from the manually measured value by only 1.2% and the length measurement by 1.4%. It is also possible to detect anomalies in the process, such as balling effects.

Keywords: Additive Manufacturing, PBF-LB/M, Process Monitoring, High Resolution, Balling Effect

Introduction

In the realm of advanced manufacturing technologies, powder bed fusion using a laser (PBF-LB) [1] has emerged as a game-changing process, revolutionizing the production of complex and customized metallic components. PBF-LB is an additive manufacturing technology that utilizes a high-powered laser beam to selectively fuse metal powder. The exposure is repeated layer by layer until a three-dimensional object is created. [2–4] Thereby, the process has a high potential for weight reduction and the production of customized workpieces with a batch size of one, making it particularly suitable for aerospace or medical applications [5, 6]. In view of small quantities, predictive and holistic quality assurance is required. However, the PBF-LB process is susceptible to various defects that can compromise the integrity and quality of the final product. To mitigate these challenges, the implementation of robust process monitoring systems has become imperative and more knowledge must be gained about the origin of such defects. This contribution demonstrates an approach to gain deeper knowledge about the defect emergence. Thereby, the used system is based on a high-speed camera with high magnification where the gained data is evaluated automatically with a Python script. Overall, the method should initially help to detect geometrical or cooling anomalies of the melt within individual scan tracks.

During the PBF-LB/M process, specific irregularities of the melt track as balling or even specific defects within the bulk material, like lack of fusion (LOF), gas pores or thermal stress-induced cracking can arise. All listed phenomena and voids in the bulk material can lead to unstable processes or even structural weaknesses and reduced mechanical properties in the manufactured components [7–13]. Thus, it is needed to understand the emergence of these defects. In many studies, the occurrence of defects and their shape is investigated in dependence on the used process parameters like the laser power P_L, scan velocity v_S or layer height d [14–16]. Figure 1 provides an overview of the process parameters investigated by Gordon et al. [13]. Also shown are the volumetric data obtained by micro computed tomography (mCT), and the derived thresholds indicating the occurrence of gas pores or LOF defects. As in the other studies, Gorden et al. found that LOF occurs when the set volumetric energy input is reduced, while gas pores occur when the applied volumetric energy is increased.

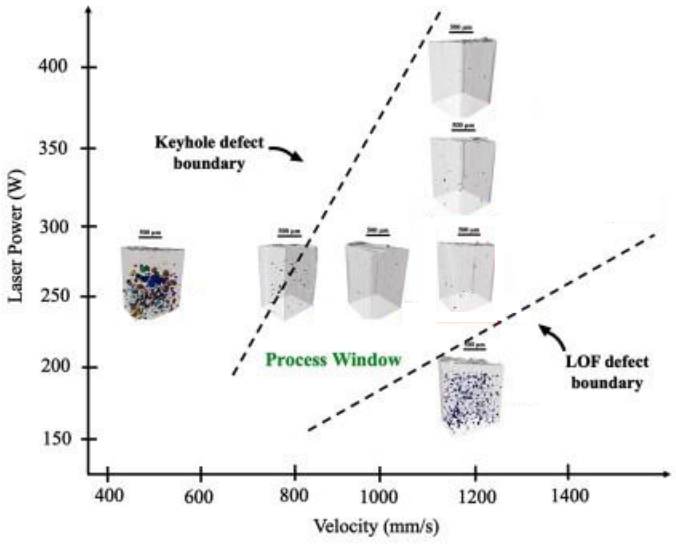

Figure 1 –mCT data of PBF-LB/M manufactured specimen over the used process parameters – boundaries for the occurrence of defect types of LOF and gas pores [14].

Although optimal process parameters are determined for material processing, implying a defect-free fabrication of parts, localized defects can still manifest. This can be attributed to various influencing factors that increase or decrease the energy input into the material volume. An example of reduced energy input and thus the occurrence of LOF is the interaction of the laser beam with process by-products, such as metal vapor or metal particles in solid or liquid form, which are stirred up during the process. [17, 18] Ladewig et al. [18] stated that even balling effects can occur depending on the laser-metal vapor interaction. The balling behavior of 316L stainless steel processed on a self-developed SLM machine with a 200 W laser was investigated in dependence of serval factors by Liu et al. [19]. Thereby, among other things, they stated, that the behavior is dependent on two factors, the set laser power P_L but also on the layer height d respectively on the amount of material that must be melted. The influence of parameter variations on single tracks are shown in Figure 2a) and b). In Figure 2c) the consequences of balling at a local point within one layer are shown, where melt tracks do not overlap and thus gaps arise. These then can lead to defects like LOF. Based on the Figure 2, it can be considered that the melt pool geometry changes

if the process conditions vary. Since the effect of balling has a direct influence on the resulting material properties and the process stability, the occurrence of balling should be avoided.

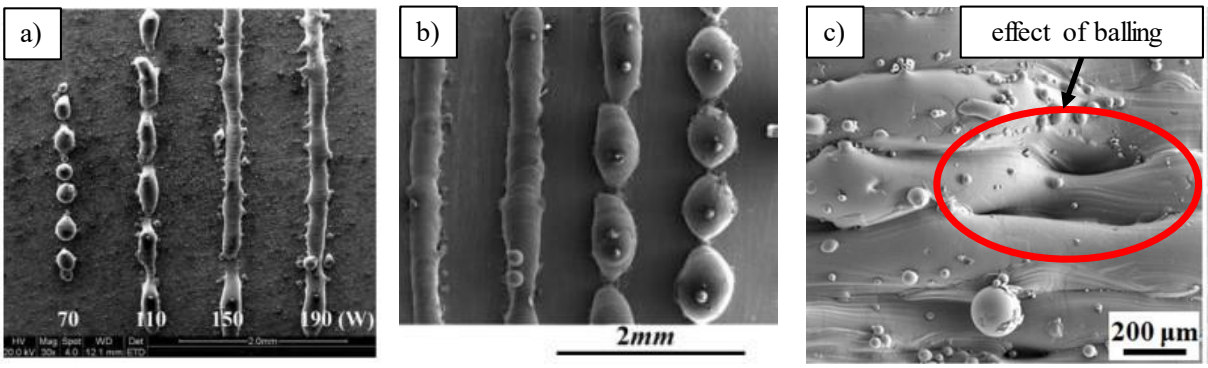

Figure 2 - Balling behavior of 316L stainless steel a) in dependence of set laser power P_L; b) layer height d (both from [19]); c) Expression of balling within a layer [20].

However, it is not possible to avoid the occurrence of balling totally. To minimize the production of parts with these defects, it makes sense to develop monitoring systems that can detect changes in the melt pool geometries during the process and take corrective action. As Grasso et al. [21] reviewed, there are many different approaches to monitor the PBF-LB/M process in situ, based on various methods. Thereby, five levels of process monitoring are introduced, as shown in Figure 3. Level 0 offers the lowest resolution of local phenomena, and level 4 is the highest. Level 3 defines measurements, with the highest level of detail and thus the melt pool dynamics. In their work, they also stated that most of the publications about in situ measurement systems referred to systems in level 2 with over 34% followed by level 3 with 26% in the years from 2018 - 2020. The high percentage (51%) of publications looking at the process in Levels 2 and 3 shows that there is still a need to gain more knowledge there. Goossens et al. [22] have developed an approach for analyzing melt pool widths using data captured by a coaxially aligned high-speed camera. During the experiments, an EoSens® 3CL high-speed camera from Mikrotron GmbH was used to generate videos with a frame rate of 20,000 FPS, corresponding to a shutter time of 50 µs, and a spatial resolution of 11.8 µm x 11.8 µm per pixel. It has been demonstrated that the widths of melt pools, produced using varying combinations of process parameters (scan speed ranging from 400 mm/s to 1100 mm/s; laser power ranging from 100 W to 600 W), can be determined with an average error of -2.8% and a standard deviation of 18.5%. However, it has also been shown that melt pool widths can be underestimated by up to -54.05% or overestimated by up to 35.59%, depending on the parameter combination. The authors also acknowledge the coarse resolution as a potential

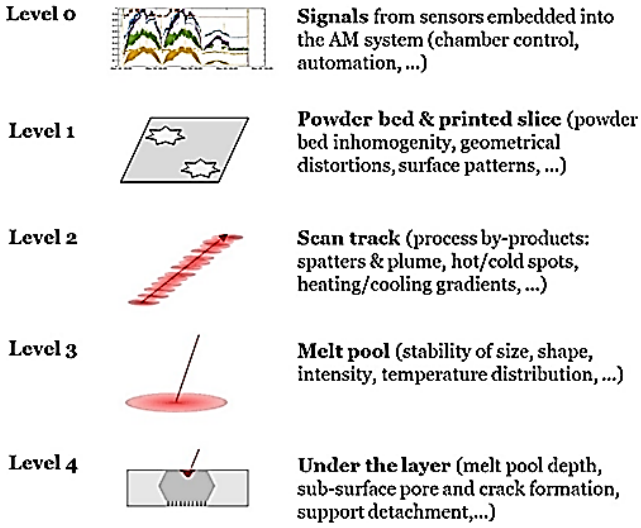

Figure 3 - Different levels of measurements in the PBF-LB/M process according to Grasso et al. [21].

source of error and refer to the ratio between the spatial resolution of a pixel and the expected melt pool width, which is 10.32%.

In this contribution, a system is developed and applied which can be classified as level 3 due to its high temporal (40,000 frames per second acquisition rate) and spatial (1.44 µm x 1.44 µm per pixel) resolution to overcome high standard deviations. According to Grasso et al. [21] and recent studies, the spatial resolution, particularly when combined with the temporal resolution, corresponds to the highest resolution that has been used so far for investigating the melt pool dynamics or geometry in PBF-LB/M.

Methods

Evaluation approach

To understand the underlying mechanisms in the defect formation, a method to investigate the melt pool morphology of individual scan vectors in the PBF-LB/M process was developed. For this purpose, a high-speed camera system (HSC system) is employed to record in situ, temporally, and spatially high-resolution videos during the exposures in PBF-LB/M. Subsequently, this data is analyzed regarding the width, length, and cooling time of the melt tracks with a self-developed Python script. The hardware and software used as well as the basics of the calculation are presented below.

Test Bench

The experimental setup used to analyze the melt pool dynamics on a PBF-LB/M system with a high-speed camera (HSC) system is depicted in Figure 4. It illustrates all the key components along with their respective positions.

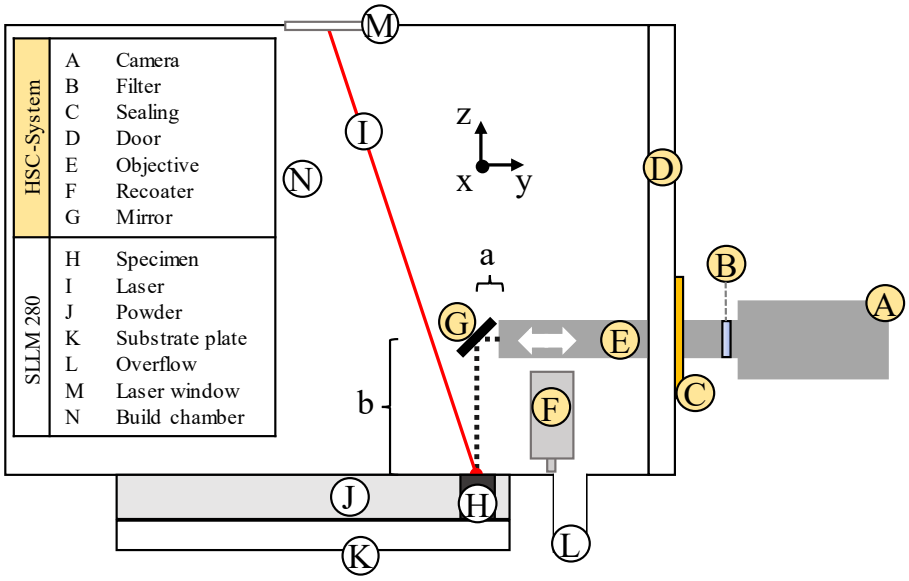

Figure 4 - Schematic representation of the experimental setup for recording the melt pool dynamics using a high-speed camera.

All investigations presented in this paper are carried out on an SLM 280 Hl 1.0 **PBF-LB/M System** manufactured and distributed by SLM Solutions AG. The system is equipped with two independent lasers which operate at a wavelength of 1,064 nm. Each laser is capable of emitting a maximum power of 700 W. The laser focal point diameter d_L can be adjusted between 80 µm and 115 µm and is set to 90 µm for these experiments. Nitrogen is used as the process gas to evacuate the

oxygen content during the processes as much as possible, but at least below 0.1 % to minimize the influence of oxidation. The gas flow is directed in negative x-direction (see Figure 4). [23]

For the melt pool analysis, a Nova Fastcam S6 **High-Speed Camera** Ⓐ, manufactured by Photron GmbH, is utilized. It is mounted horizontally on a bracket (not depicted in Figure 4) that enables shifting in a small range in y-direction. The camera is equipped with a 20.48 mm x 20.48 mm large image sensor, which resolves at 1,024 pixels x 1,024 pixels, resulting in a size of 20 µm x 20 µm of each. The monochrome image sensor offers a high light sensitivity of ISO 64,000. The maximum frame rate of the camera at the highest resolution is 6,400 frames per second (FPS) but can be increased up to 800,000 FPS by reducing the utilized number of pixels. In the monochrome version of the camera, the intensity of light hitting the sensor is outputted in values ranging from 0 for a black pixel to 255 for a white pixel. If the detectable intensity falls below or exceeds these values, the respective pixel will output a value of 0 or 255. An overview of the resolution in relation to the maximum FPS and the resulting shutter speed is provided in Table 1. [24]

Table 1 – Maximum usable resolution and shutter speed of the HSP system in dependence on the chosen FPS

FPS in 1/s	Resolution	Shutter speed in µs
6,400	1,024 x 1,024	154.2
20,000	1,024 x 336	48
40,000	896 x 176	23
80,000	640 x 112	11.1

An SP785 Near-IR Dichroic **Shortpass Filter** Ⓑ, provided by Midwest Optical Systems Inc., is utilized to reduce stray radiations during the analysis of melt pool intensities. The specified wavelength range in which radiation is transmitted with over 90 % efficiency is between 425 nm and 770 nm. Less than 0.02 % of the intensity emitted by the SLM 280 HL laser is transmitted through this filter. [25]

A 12X Distance Macro Zoom Lens, manufactured by Navitar Inc., is used as the **objective** Ⓔ. The combination of camera and objective enables magnification and thus high-resolution imaging of the field of view (FOV) with $r_{HSC} = 1.44$ µm/pixel. The working distance a_W of the entire system, which is the sum of the value a and b (see Figure 4), is adjustable from 73 mm to 85 mm. [26]

Due to the small a_W and thus height b, it is not possible to use the original recoater of the SLM 280 system. For this purpose, a customized **recoater** Ⓕ with a lower height was developed to enable recoating within the process.

Since the camera and the objective are aligned horizontally, a **mirror** Ⓖ is needed to redirect the radiation path. Therefore, a silver-coated quartz glass substrate with a surface flatness of λ/20 was used. The mirror reflects incident spectral radiation with wavelengths ranging from 450 nm to 10,000 nm with over 98% efficiency. [27]

Since the lens is positioned inside the **build chamber** Ⓝ, the point where it enters the build chamber through the door Ⓓ of the SLM 280 HL had to be sealed. This is to ensure that the process conditions do not deviate from those of other processes. For this purpose, a **seal** was designed and manufactured using the MEX process - shown in Ⓒ.

Approach to evaluation

The evaluation of the melt pool widths b_S and lengths l_S is based on Planck's radiation law, which states that black bodies radiate with the power P_I depending on their own temperature T. The spectral radiance, $M_\lambda^0(\lambda, T)$, of a black body can be determined based on Equation 1 after wavelength representation. [28–30]

$$M_\lambda^0(\lambda,T)dAd\lambda = \frac{2\pi hc^2}{\lambda^5}\frac{1}{e^{hc/\lambda kT}-1}dAd\lambda \quad \left[\frac{W}{m^3}\right] \tag{1}$$

h	Planck constant	Js	λ	Wavelength	nm
c	Speed of light	m/s	k	Boltzmann constant	J/K
A	Area	mm^2	T	Temperature	K

$M_\lambda^0(\lambda,T)$ thereby represents the emitted radiant power of a defined area A of a black body within a wavelength range $d\lambda$. For a gray body or a selective radiator, which neither absorbs nor emits the total incident radiation, the $M_\lambda^0(\lambda,T)$ must be corrected by multiplication with a factor, the emissivity ε. The observed material, EOS 316L [31], does not have the properties of a black body, so the value of ε is needed to correlate the temperature with the intensities. Since the determination of ε is complicated caused by the temperature- and wavelength dependence, a direct correlation of the intensities detected by the camera and the real temperature is not carried out in this study. However, it is possible to distinguish between solid and molten material in the HSC videos and thus clearly identify the point at which the material property changes. When this point is detected, the intensity can be correlated to the melting or solidification temperature of the material. From there, the width and length of the melt pool can be determined. Since this method is based on the assumption, that the detected intensity is just caused by the radiation of the melt pool, it is important to evaluate and minimize the influence of other radiations or reflections. Thereby, the reflection of the PBF-LB/M laser must be considered. In Figure 5 the wavelength-dependent relative spectral response of the camera sensor and the transmission of the filter are plotted. To be able to compare these functions, both are plotted as the value effective intensity I_E, where this value describes how

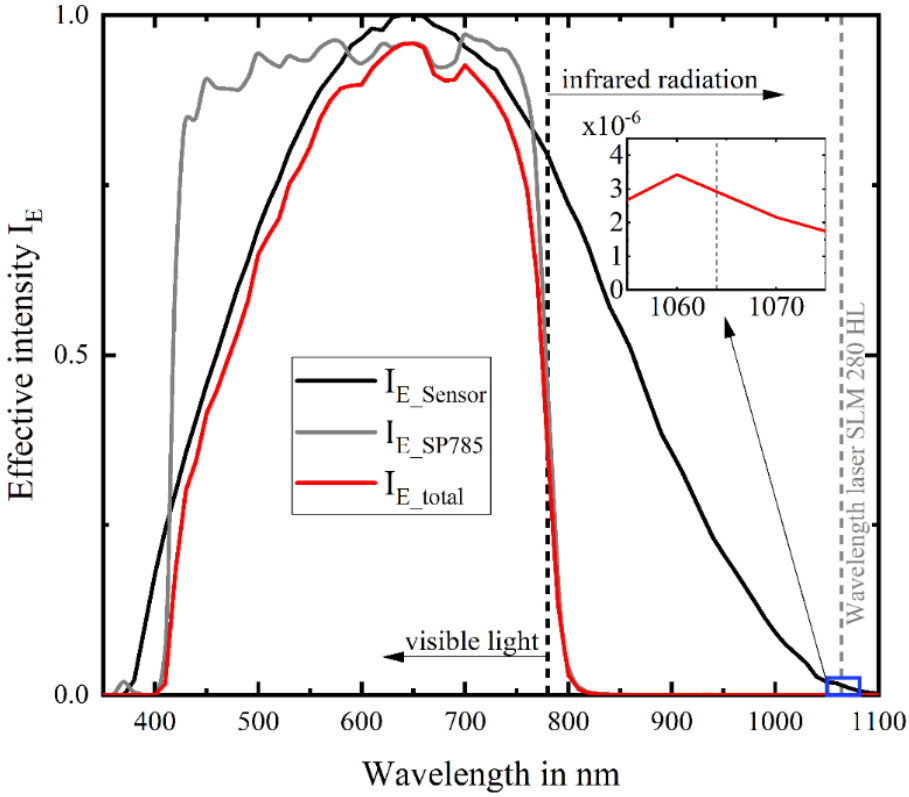

Figure 5 - Effective intensities the camera sensor, the SP785 filter and the whole HSC-system, taken from [24, 25].

much of the emitted intensity of a specimen can be detected. For an evaluation of the total I_E of the HSC system both functions I_{E_Sensor} and I_{E_SP785} are multiplied. The result is given as the red line, where it can be shown that the intensity of the PBF-LB/M laser can be detected by the cameras sensor with just $2.5x10^{-4}$ %. Thus, the influence of the laser for the evaluation of the melt pool geometry can be considered as negligible. Similarly, the use of filters can prevent damage to the camera's sensor.

Data analysis with Python script

To automate the analysis of the HSC data, a Python-based image analysis script was developed. This section describes the functionality of this tool. Overall, the script allows the determination of the following properties:

1. Melt pool width b_S.
2. Melt pool length l_S.
3. Duration of liquidus phase $\Delta\tau$.

Before presenting the evaluation methodology, an overview of the database used is given. Therefore, Figure 6a) shows an image from a video taken in this study that was evaluated with the script. During the data acquisition for the analysis of the melt pool geometry, no external illumination is applied to the FOV in order not to influence the radiation effects of the melt pool. The scan vector in the x-direction, which indicates the laser exposure direction, is marked, as well as the coordinate system which is identical to that of the PBF-LB/M system, as shown in Figure 6a). Based on the coordinate system, the extent of b_S is defined by Δy, and l_S is defined by Δx. Therefore, it is necessary to consistently record the videos in the same orientation for such an

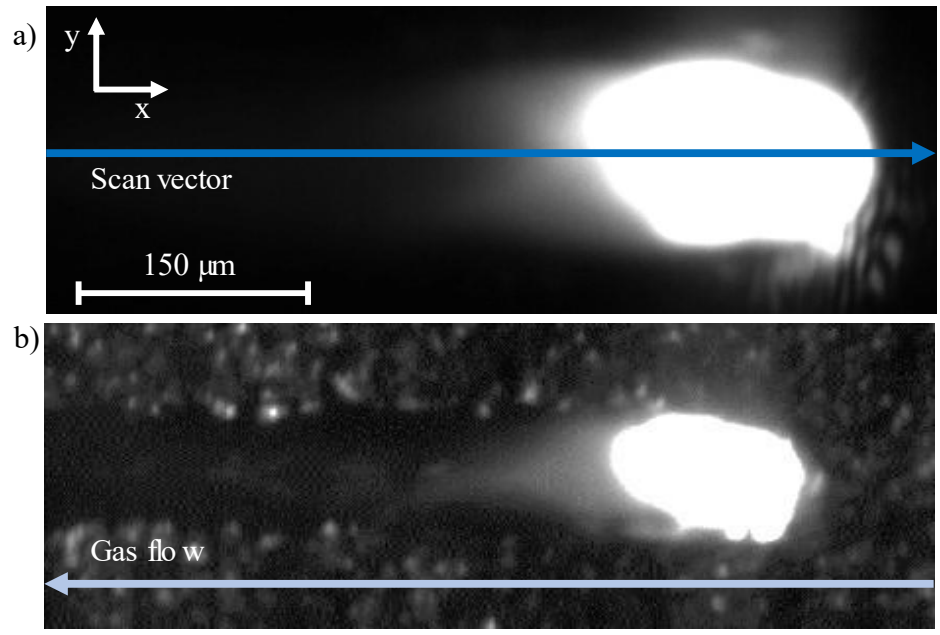

Figure 6 - Images recorded during exposure of a single scan vector, a) without illumination as used for the experiments; b) with illumination to illustrate the melt path widths to be measured.

evaluation. Additionally, in Figure 6b) a frame is shown which was taken while the FOV was illuminated with an external light source. This allows the resulting melt pool width and length to be determined by manual measurements, which results then are used to calibrate the Python script.

In the first step, the videos processed by the Python script are analyzed in terms of the occurring intensities $I_{x,y}$. For this purpose, the intensity is analyzed for each pixel $P_{x,y}(\tau)$ for each frame $1 \leq \tau \leq \tau_{max}$ and stored in a matrix. This matrix serves as the basis for evaluating the selected properties.

The **melt pool width $b_S(x)$** in µm is analyzed for each column of pixels $1 \leq x \leq x_{max}$. Therefore, the parameter I_{mel} is introduced. I_{mel} represents a material-specific intensity above which it is assumed that the material is in a molten state. For the determination of I_{mel} a single track is generated using the standard process parameters for processing EOS 316L on an SLM 280 HL machine while the HSC system is used to gain a dataset of the process. After exposure of the vector, an image of the generated welding track is taken while the FOV is illuminated with a light source, comparable with Figure 6b). Thereby, it must be ensured, that the melt track is clearly visible. Based on this image, n_m measurements of the melt pool width are executed, and with these, the mean value b_{real} and standard deviation σ_{real} are determined. Then, the obtained dataset of the HSC system is evaluated using the Python script, iteratively substituting a value for I_{mel}. After each evaluation, the detected b_s is compared with the b_{real}. Once the deviation between b_s and b_{real} has reached the lowest possible value, I_{mel} is applied.

To determine the b_s, the number of connected pixels $\Delta y(x, \tau)$ in the y-direction is analyzed in each column x and for each frame τ, that exceed the defined value of I_{mel}. Then, the highest value of Δy_{x_i}, described as $\Delta y_{x_i,max}$, which was analyzed in all analyzed frames at each x-position is used to determine the b_s according to Formula (2).

$$\boldsymbol{b_{S,x_i}(x) = \Delta y_{x_i,max}(x,\tau) \cdot r_{HSC}} \tag{2}$$

Thereby, r_{HSC} denotes the resolution of the camera system, with r_{HSC} = 1.44 µm/pixel. An example for a determination of a melt pool width at one x-position is given in section 'Results'.

To determine the **length of the melt pool l_S** in µm, the evolution of $I_{x,y_S}(\tau)$ along a line profile, in this case, the scan vector, is examined. The essential condition for evaluating the melt pool length is similar to that of b_S, where the intensity must initially satisfy the condition $I_{x,y_S}(\tau) \geq I_{mel}$. Subsequently, the number of frames, $\Delta\tau_{x_i,y_S}$, is determined until the intensity value falls below an intensity where the material is in the solid phase again. The calculation of l_S is then performed using Equation 3.

$$\boldsymbol{l_{S,y_S} = \frac{\Delta\tau_{y_S} v_s}{FPS}} \tag{3}$$

Thereby, $\Delta\tau_{y_i}$ is multiplied by the scan velocity v_s and divided by the applied frame rate FPS. As a result, it represents the calculated melt pool length of each pixel along the scan vector. To validate the results of the determination of the l_S and thus correct choice of I_{mel} videos are taken and the datasets analyzed by the Python script. Furthermore, high-speed videos are recorded, where the same external light source as for the investigation of b_S is used to illuminate to FOV. With these videos, the l_{real} can be determined manually by observing the solidification points of the melt pool. Examples of this method are given in section 'Results'.

In addition to determining the melt pool lengths, $\boldsymbol{\Delta\tau_{x_i,y_i}}$ can also be used to assess the duration of the material being in a molten state at a defined position $P_{x,y}$. Evaluating this time span, which is given in frames, can provide insights into local anomalies. Therefore, this value is

determined for each pixel in the dataset as described before and plotted in graphs which indicate different $\Delta\tau_{x_i,y_i}$ with a color scale.

Measurement Methods

Table 2 - Used process parameters of the PBF- and HSC-system

Parameter		Set 1	Set 2	Set 3	Set 4
PBF-LB/M Process	P_L	170 W	200 W	260 W	320 W
	v_S	800 mm/s			
	h	0.1 mm			
	d	0.03 mm			
	d_L	0.09 mm			
	Material	EOS 316L [31]			
	Process gas	Nitrogen			
	Oxygen level	$\leq$ 0.05 %			
HSC System	FPS	40,000			
	Shutter speed	23 µs			
	Pixel used (x,y)	896 x 176			
	Resolution	1.44 µm x 1.44 µm per pixel			

For the investigations in this paper, four parameter combinations are utilized for the PBF-LB/M process, all of which are presented in Table 2. Parameter set 2, which is the standard parameter set for the manufacturing of 316L, is used to determine the value of I where the material melts, as described before. Parameter sets 1 through 4 are then used to validate the results of the script-based melt pool width analysis. Thereby, the determined I is used to evaluate the data with the Python script. The width of the scan tracks are also evaluated with microscopes for comparison.

Parameter set 4 is applied in experiments where defects, specifically the balling effect, are provoked in single scan tracks. The increased energy input, while keeping other conditions constant, forms the basis for these experiments.

For all experiments carried out, the parameters to record the videos with the HSC system are the same. As described, a high magnification which results in a resolution of 1.44 µm x 1.44 µm per pixel is used while taking 40,000 frames per second. With this and the given scan velocity v_s it can be determined that the movement of the laser is 20 µm per frame.

Results

Calibration of the width measurement

Typical intensity profiles which arise if the intensity is determined along a line profile for consecutive frames from $t_1 = 0\ \mu s$ to $t_4 = 225\ \mu s$ are shown in Figure 7. Thereby, the profiles were obtained along the green line marked in the image, which is aligned in the y-direction with a constant value for x_i. It can be observed that the values of the intensity profiles decrease for consecutive frames. This effect can be attributed to the cooling of the melt pool at the given position with advancing time and distance between the evaluated line and the laser spot. The intensity threshold I_{mel}, which must be calibrated, is represented by a red vertical line. If the measured I exceeds this value, the material can be determined as in the liquid state, below as a solid. The value of $I_{mel} = 149$, whose calibration is described in the next paragraph, and can be used to determine the melt pool width b_S. Therefore, the furthest intersection points ($\Delta y_{x_i,max} = y_2 - y_1$) between the intensity profiles and the threshold line are identified, as explained in section 'Measurement Methods'. In this case, the $b_S = 114.98\ \mu m$ is determined by analyzing the intersections of the intensity profile in frame $t_1 = 0\ \mu s$. Overall, it can be seen that an increase of the value of I_{mel} results in smaller determined melt pools, while a decrease of I_{mel} leads to an increase in the determined width. It is evident from the shape of the intensity profile that the intensity variations at the edges of the melt pool are approximately symmetric. For an accurate determination of I_{mel}, it is not sufficient to examine only one x_i-position of the melt pool; instead, all determined widths for each x-position should be considered.

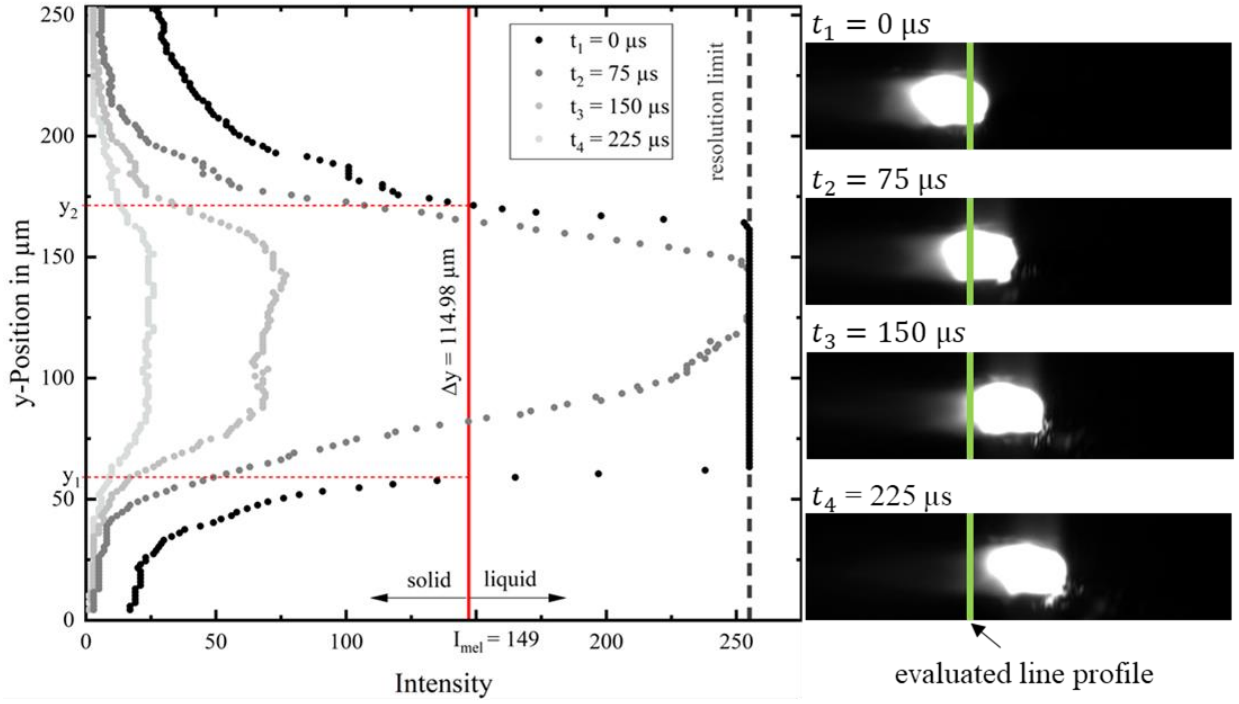

Figure 7 - Intensities along a line profile directed in y-direction in different frames in the process.

In Figure 8, all analyzed $b_S(x_i)$, which were determined using the calibrated value for I_{mel}, are depicted as black dots. $I_{mel} = 149$ was determined as described in section 'Measurement Methods'. Therefore, the actual melt pool width b_{real} and the standard deviation σ_{real}, were determined to be $b_{real} = 119\ \mu m \pm 9\ \mu m$ while using an image, taken with the camera while the

FOV was illuminated, also according to section 'Measurement Methods'. This image and the measurement lines are depicted in Figure 8. The mean value and standard deviation are represented by the red line and the red dashed lines, respectively. It can be observed that the widths determined by the script with $b_S = 117.12\ \mu m \pm 2.52\ \mu m$ is within the range of the $b_{real} \pm \sigma_{real}$. Overall, these results suggest that outliers in the melt pool widths are slightly underestimated to some extent by the Python script. Thereby, the lower σ_S can be attributed to the reduced error that occurs in this measurement. When manually measuring b_{real}, human errors such as subjective placement of the start and end points or slight shifts during positioning or variations in illumination must be considered. Also, the number of measurements carried out is much lower than in the Python-based analysis, so the influence of maxima and minima on the b_{real} could be disproportionate. In this case, the deviation between b_s and b_{real} is quite low at 1.2%. Therefore, the calibration performed can be considered successful, as well as the approach to use the parameter I_{mel} to evaluate melt pool width.

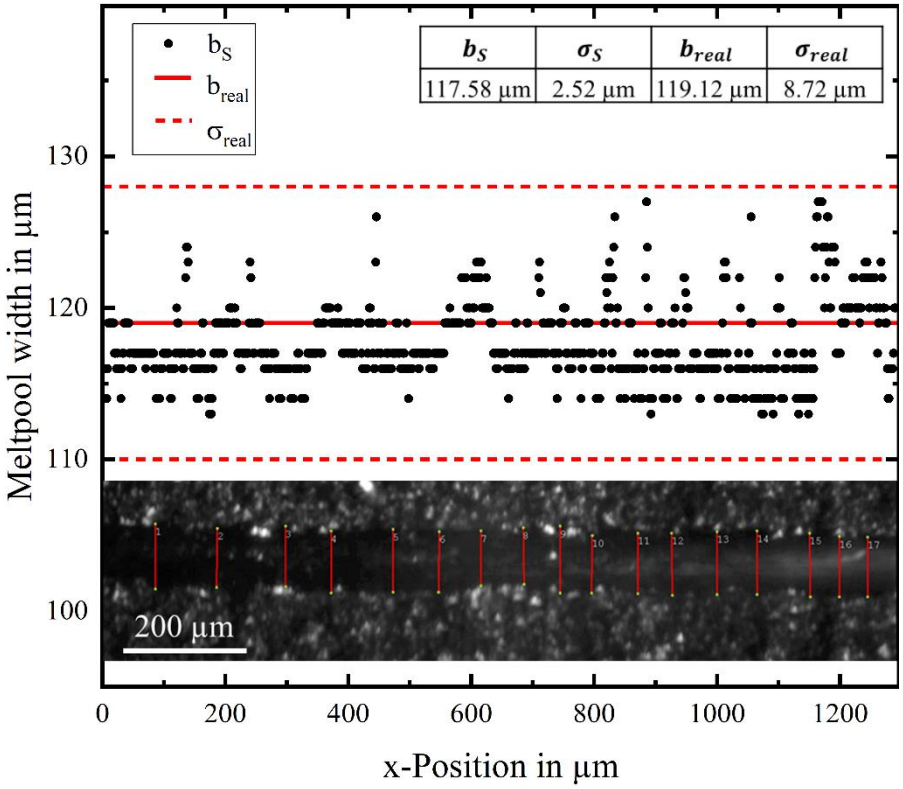

Figure 8 – Melt pool width determined by the Python script ($1 \leq x_i \leq 896$), at the bottom a image where the melt pool width was measured manually (bottom).

Validation of the width measurements

To validate the functionality of the script-based evaluation of melt pool widths, new data sets are generated while exposure of single tracks using the four parameter sets presented in Table 2. The widths of the melt pools were initially determined using the Python script with the value for *I* defined in the previous section. Subsequently, a manual analysis of the melt pool widths was conducted using a microscope for comparison. The results of these evaluations are shown in Figure 9 as b_S and b_{real}, but also as frames of each evaluated data set. The width corresponses as expected and in accordance with various studies, as described by Metelkova et al. [32] for example:

The lowest laser power setting resulted in the smallest melt pool width, while the melt pool width increased with higher laser power. Furthermore, it is evident that the standard deviation increases as the selected P_L deviates further from the standard parameter set for the processing of 316L due to the occurrence of variations in the melt track like balling.

Even though $b_{real\_set2} = 116.99 \pm 6.84$ µm is slightly lower in this experiment compared to the result of the calibration measurement ($b_{real\_cal} = 119.12 \pm 8.72$ µm), the deviation between $b_{real\,set2}$ and $b_{S\_set2} = 115.73 \pm 3.16$ µm is only 1.09%, which is even lower than during calibration. Similarly, it is observed that the discrepancies in varied parameter sets in these investigations are at most 1.72%, as seen in the width result of parameter set 4. Overall, the results of b_S and b_{real} for each parameter set provides that the determined value for I is suitable for the analysis of additional datasets where the same base material is used.

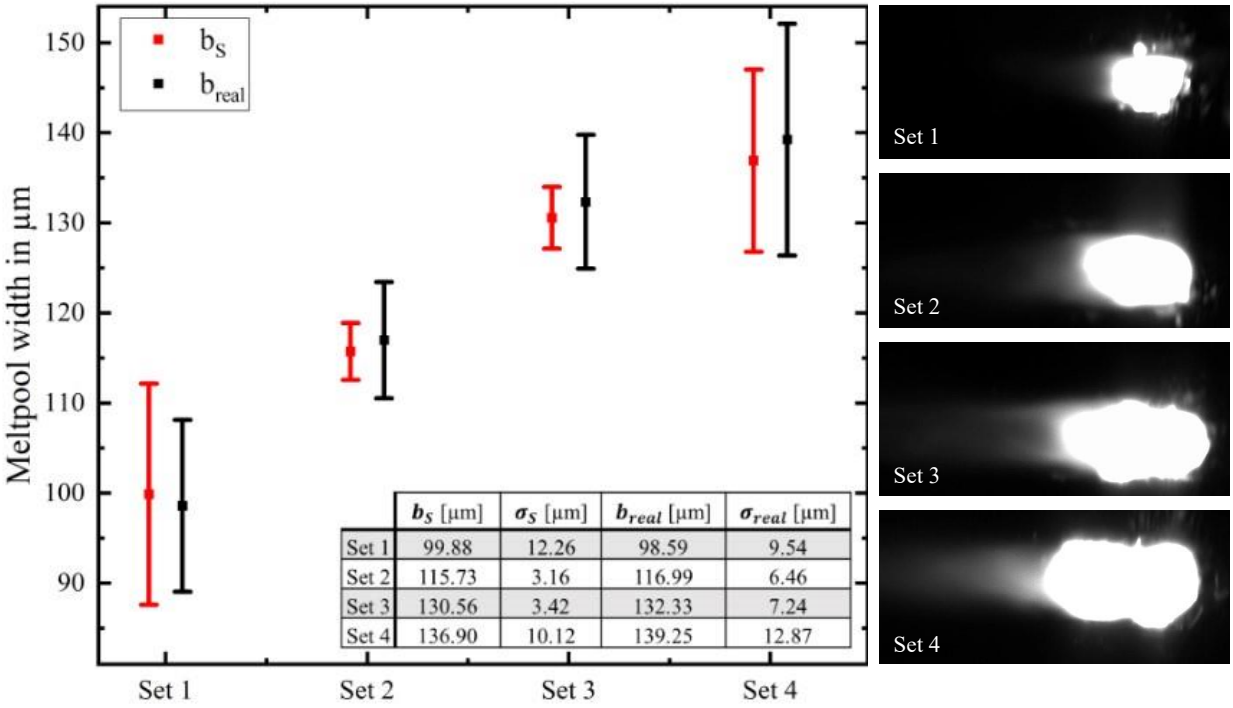

	b_S [µm]	σ_S [µm]	b_{real} [µm]	σ_{real} [µm]
Set 1	99.88	12.26	98.59	9.54
Set 2	115.73	3.16	116.99	6.46
Set 3	130.56	3.42	132.33	7.24
Set 4	136.90	10.12	139.25	12.87

Figure 9 – Python based measurement versus manual measurement of widths.

Calibration of the length measurement

In Figure 10, three frames from a video and their corresponding intensity profiles over the x-position in the FOV are shown. Based on the intensity profile at time $t = n_2$, the complete cycle of the exposure of a single track can be inferred. Material that has not been exposed by the laser exhibits an intensity value of I = 0 ($x \geq 1{,}000$ µm). Material closer to the laser is preheated, leading to increasing radiation emission (890 µ$m \leq x \leq 1{,}000$ µm). Once the emitted radiation exceeds the sensor's capacity at a certain temperature, an intensity value of 255 is recorded. During the laser exposure and a certain trailing period, a plateau is formed with $I = 255$ (600 µ$m \leq x \leq 890$ µm). As the material cools down, the detected I decreases, where the decrease can be approximated exponentially (0 µ$m \leq x \leq 600$ µm).

In Figure 10, I_{mel} is also represented as a red horizontal line. The value of $I_{mel} = 149$, which was determined iteratively in advance, is also used for evaluating the melt pool length. The figure illustrates how the melt pool length can be determined $\Delta x_{mel} = x_2 - x_1 = 277.5$ µm. Also,

a new intensity value I_{sol} is introduced in Figure 10 as a blue horizontal line and describes the intensity at which the material solidifies after the liquid phase. The need to use this value can be derived from Figure 11.

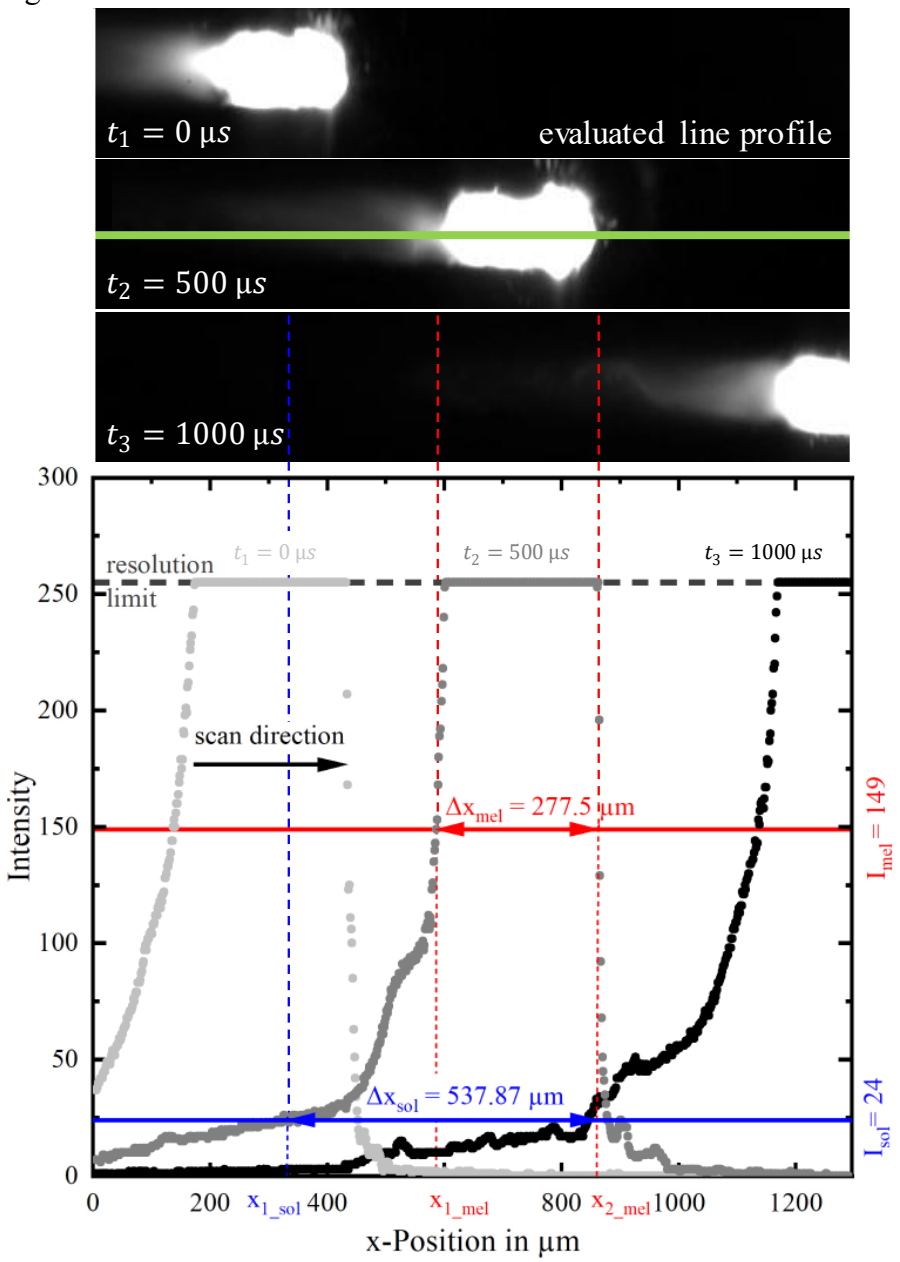

Figure 10 – Three intensity profiles, evaluated along the scan vector and used intensities to determine the melt pool length.

It shows the results of the determined l_{s_mel}, l_{s_sol} and l_{real}. Also depicted are three consecutive images taken during the exposure of a single track while illumination was activated which were used for the manual determination of l_{real} values. Distinctive spots on the melt pool were analyzed and evaluated from the point when they no longer showed any change. In this case, a point with significantly increased intensity due to reflection of the illumination intensity was used as a distinctive spot. At $t = 0$ µs, this point is not visible but appears at $t = 25$ µs. Since in the next

frame (t = 50 µs) and all the following ones no change of this point can be detected, it can be concluded, that the material is solidified. The mean value of l_{real} = 533.12 µm ± 28.02 µm was determined with more than 15 measurements in different videos. When selecting the videos or areas to be measured, care was taken to ensure that a concise change in the melt pool geometry could be investigated in each case, as shown in Figure 10. This prevents subjective perceptions from having a major influence on the results. With the Python script and I_{mel} = 149, which was determined for the melt pool width, an l_{S_mel} = 277.51 µm ± 40.21 µm was calculated. The high deviation between the manually and Python-based determined melt pool lengths of 255.61 µm or 52 % suggests that I_{mel} = 149 cannot be used for the detection of b_S and l_S. Therefore, another intensity, referred to as I_{sol}, was introduced, as shown in Figure 10. The length of the melt pool is subsequently calculated using the formula $\Delta x_{sol} = x_{2\_mel} - x_{1\_sol}$. Thereby, the I where material melt is chosen as before, just the intensity where material changes from liquid to solid state is corrected. After incorporating these conditions into the Python script and applying I_{mel} = 149 and I_{sol} = 24, the value of the lengths can be determined as l_{S_sol} = 540.37 µm ± 36.72 µm. The deviation between L_{s_sol} and l_{real} is lowered with this approach to 7.25 µm or 1.4 %.

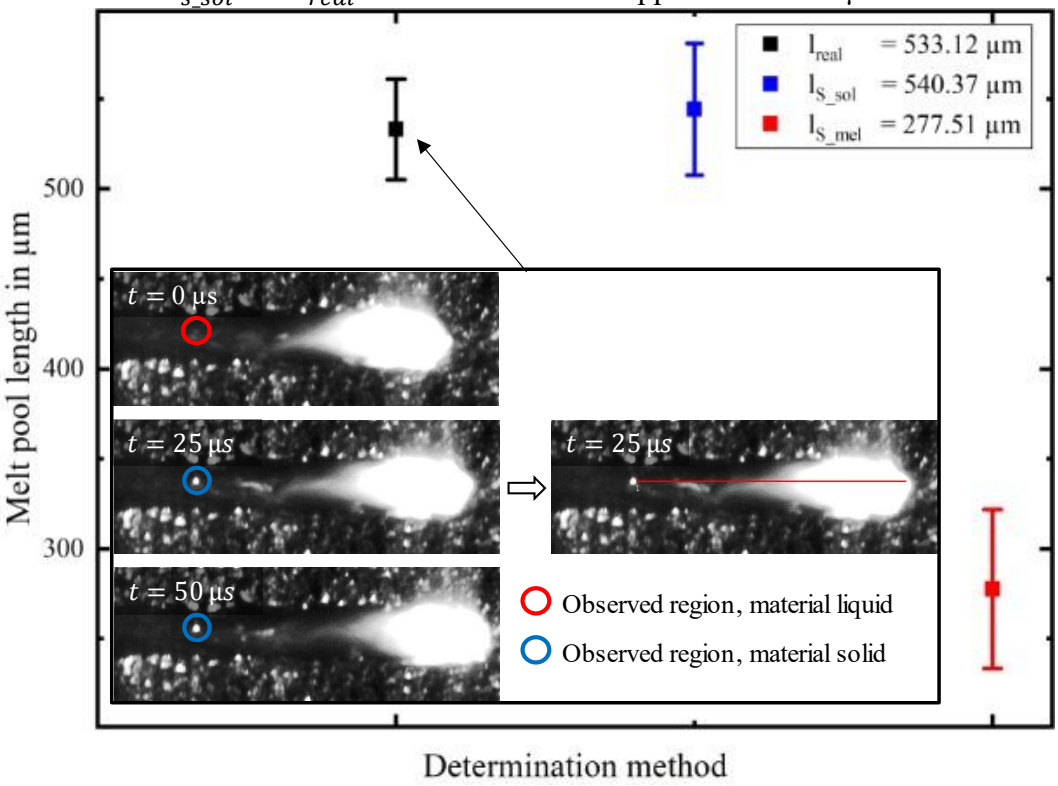

Figure 11 – Results of manual and Python based determination of melt pool lengths with example images for the manual analyzation.

The application of the methodology that the melt intensity is not equal to the solidification intensity may initially seem unusual. However, the varying intensities can be caused by the solidification range of an alloy. Alloys melt (liquidus) and solidify (solidus) at different temperatures, with the liquidus temperature being higher than the solidus temperature. Furthermore, mechanisms can arise that lead to an undercooling of the melt and thus increase the temperature respectively intensity difference [33, 34]. Another factor contributing to the unequal intensity values could be the influence of the systems laser on the detected intensities, despite the

high radiation filtration, compared to Figure 5. Interferences of melt intensities are also possible in the vicinity of the region where the laser exposes the material, as the irregular geometries of the melt pool promote such occurrences. A Validation of this method as described for the width is still pending at this time. However, the presented method offers a good approach for automated length determination.

Cooling duration

Besides evaluating the melt pool lengths, the cooling time $\Delta\tau_{x,y}$ can also be calculated for each dataset with $\Delta\tau_{x,y} = \tau_{I\_sol} - \tau_{I\_mel}$. The result of such an evaluation, where parameter set 1 was used, is shown in Figure 12. With this figure, the cooling behavior of the intensities dependent on the position in x- and y-direction can be observed. Furthermore, it is possible to give information about the local intensity change and therefore relative temperature in the melt pool. Overall, the solidification of the material starts at the outer edge of the melt pool, where $\Delta\tau_{x,y}$ is the smallest. As the pixel gets closer to the scan vector, the value of $\Delta\tau_{x,y}$ increases, indicating a slower solidification. The white pixels around the data are those where the intensity I_{mel} was not exceeded during the examinations, so there is no data there. Overall, a nearly symmetrical cooling can be assumed along the entire scan vector.

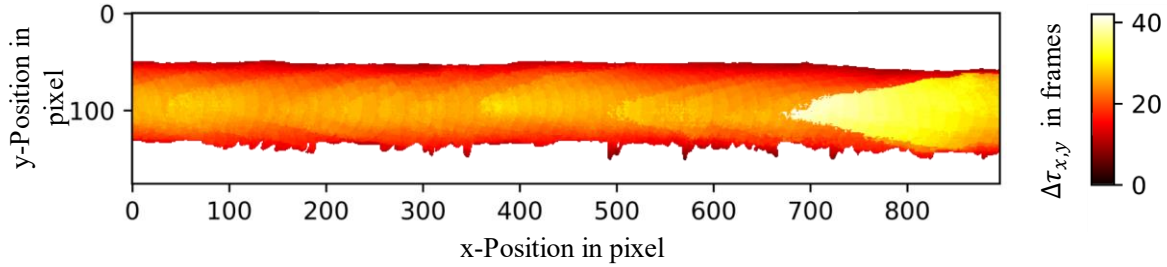

Figure 12 – Cooling duration $\Delta\tau_{x,y}$ along a scan vector, exposure and recorded using parameter set 1.

Defect analysis

To assess the system's ability to detect areas with anomalies, experiments were conducted where defects were intentionally induced. One specific defect type that is intentionally created is known as "balling." For this purpose, parameter set 2, compare section “Methods” is used. The evaluation of a dataset is shown in Figure 13. The number of frames $\Delta\tau_{x,y}$ required between the melting of a pixel and its subsequent solidification or the first occurrence of exceeding I_{mel}, followed by falling below I_{sol}, is represented using a color scale. White pixels indicate that I_{mel} was not reached. From the figure, it is evident that the cooling durations in two areas are significantly longer ($\Delta\tau_{x,y}$ >= 80 frames) compared to other areas ($\Delta\tau_{x,y}$ ~ 40 - 60). Higher $\Delta\tau$ values typically indicate regions with increased melt volume. Between these two areas, marked with red circles, there is a region where the $\Delta\tau$ values are lower. In this region, it can be assumed that the melt volume is lower. Such variations along a melt pool can be an indicator of melt pool disruptions and thus the occurrence of the balling effect.

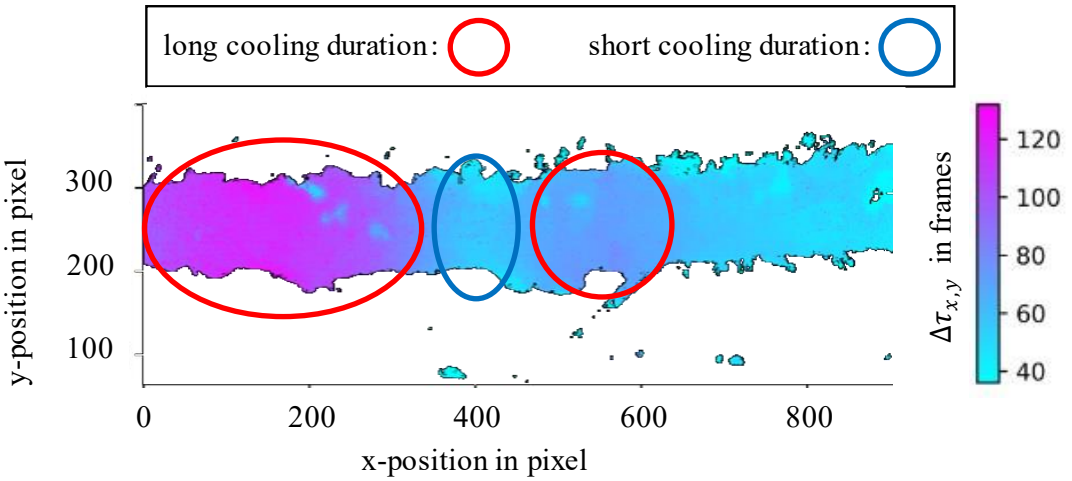

Figure 13 –Cooling duration $\Delta\tau_{x,y}$ in frames of a dataset, gained by single track exposure with $P_L = 320\,W$ respectively parameter set 2.

To investigate the hypothesis that the balling effect occurs at this location, the analyzed dataset is additionally evaluated manually. Selected frames from this dataset are shown in Figure 14. To better visualize the observed effects, they have been processed in the Photron Fastcam Viewer software using the HDR tool at level 3, which corresponds to brightening the video. The exposure level is depicted. The laser enters the field of view (FOV) from the left side and exposes the material, which subsequently melts. The melt has a higher intensity than the surrounding powder. After the laser is no longer within the FOV, melted particles can be observed being ejected through the FOV ($t =$ 2,250 µs). Subsequently, the intensity of the pixels decreases. At time $t =$ 3,600 µs, it becomes apparent that powder particles adhere to the melt, emitting significantly lower intensity. A first interruption of the intensity profile is noticeable. At $t =$ 4,850 µs, an elevated intensity is still visible in the left portion of the image. Overall, with the analysis of these images the suggestion that the balling effect occurred within the scan track could be confirmed. Furthermore, it could be seen, that the powder particles, which are connected to the melt track at $t =$ 2,250 µs influence the determination of $\Delta\tau$, compare Figure 13 (left area where light blue pixels occur in the purple region) and Figure 14. This leads to the conclusion that even small influences in the melt pool region could be determined.

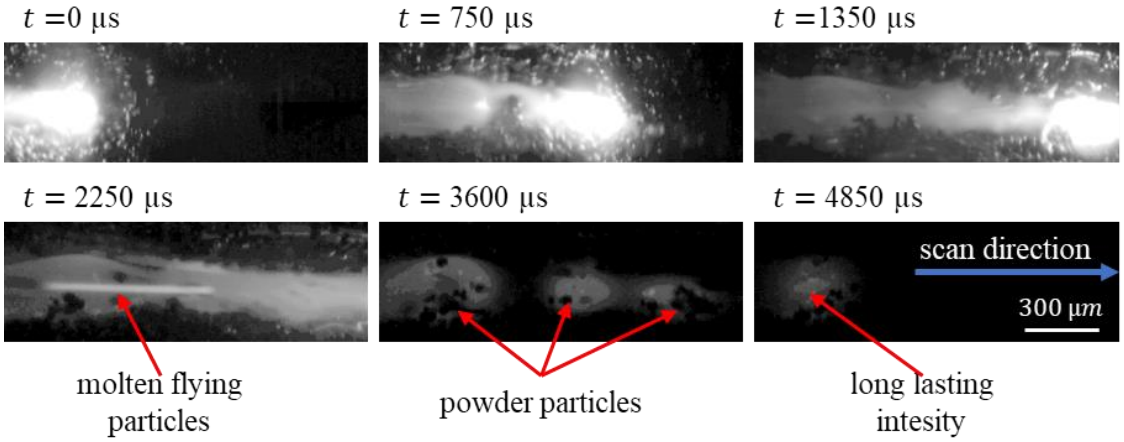

Figure 14 - Emergence of the Balling Phenomenon on a Scan Vector

Conclusion and Outlook

In this study, a method was developed to evaluate the melt pool width, melt pool length, and cooling duration of individual pixels recorded while generating melt tracks within the PBF-LB/M process. To accomplish this, the objective of the high-speed camera system was brought into the build chamber of an SLM 280 Hl machine and hermetically sealed, allowing for the capture of videos with high spatial resolution (1.44 µm x 1.44 µm per pixel) and high temporal resolution (40,000 FPS). The analysis of the acquired datasets was performed using a custom-developed Python script, which involved the manual determination of the melt and solidification intensities I_{mel} through correlation. The melt intensity was determined based on the melt pool width and validated using the length parameter. The results demonstrate that the introduction and application of an I_{mel} and I_{sol} parameter in the Python script are effective in determining geometric properties. The melt pool width was determined with a deviation of 1.2 % from the manually measured width, and the melt pool length was determined with a deviation of 1.4% using the Python script and standard PBF-LB/M process parameters.

Furthermore, it is possible to analyze cooling durations, which means the number of frames respectively time that a pixel intensity is above the defined I_{mel}. With this, it is possible to determine irregularities within the melt track, for example, if the cooling duration of a region is lower/higher than expected. With this approach, it could be shown that the occurrence of balling could be detected on single tracks.

Since the size of the datasets is quite high and the analysis of the data must be done in a sequential process, it cannot be used for real-time monitoring of the process yet. On the other hand, there are quite a lot of potential use cases for this method. In the field of fundamental research, this method might be useful to gain more insight into the process behavior during the melting and solidification of novel materials. Here, materials, where it is needed to gain more knowledge about the dynamics of the melt track or local temperature changes, can be observed in future work. For example, materials such as metallic glasses or diamond-reinforced metal matrix composites can be suitable materials to be observed, since the local cooling durations have a huge impact on crystallization in bulk metallic glasses or the graphitization of the diamonds embedded in the metal matrix [35–38]. With improvements of the script, it could also be possible to track the movement of diamonds within the melt track.

In addition, it is useful to correlate the intensities detected by the HSC system with real temperatures as Lane et al. [39] has performed. For this purpose, it would be useful to couple the system with a high-speed pyrometer within the analysis room.

Acknowledgements

The camera used in this work was funded by the Deutsche Forschungsgemeinschaft (DFG, grant number WI 2118/17-1). The PBF-LB/M machine used for this work was funded with support from the University of Duisburg-Essen and the Deutsche Forschungsgemeinschaft (DFG, grant number INST 20876/341-1).

References

[1] DIN EN ISO/ASTM, “DIN EN ISO/ASTM 52900 PBF-LB/M: Additive Fertigung – Grundlagen – Terminologie,”

[2] W. Associates, *Wohlers report 2022: 3D printing and additive manufacturing global state of the industry*. Fort Collins (Colo.): Wohlers Associates, 2022.

[3] I. Gibson, D. Rosen, and B. Stucker, *Additive manufacturing technologies: 3D printing, rapid prototyping and direct digital manufacturing*. New York, Heidelberg, Dodrecht, London: Springer, 2015. [Online]. Available: https://www.loc.gov/catdir/enhancements/fy1617/2014953293-b.html
[4] M. Brandt, Ed., *Laser additive manufacturing: Materials, design, technologies, and applications*. Oxford: Woodhead Publishing, 2016.
[5] R. Liu, Z. Wang, T. Sparks, F. Liou, and J. Newkirk, "Aerospace applications of laser additive manufacturing," in *Laser Additive Manufacturing*: Elsevier, 2017, pp. 351–371.
[6] M. Munsch, "Laser additive manufacturing of customized prosthetics and implants for biomedical applications," in *Laser Additive Manufacturing*: Elsevier, 2017, pp. 399–420.
[7] D. Kotzem *et al.,* "Impact of single structural voids on fatigue properties of AISI 316L manufactured by laser powder bed fusion," *International Journal of Fatigue*, vol. 148, p. 106207, 2021, doi: 10.1016/j.ijfatigue.2021.106207.
[8] S. Afkhami, M. Dabiri, S. H. Alavi, T. Björk, and A. Salminen, "Fatigue characteristics of steels manufactured by selective laser melting," *International Journal of Fatigue*, vol. 122, pp. 72–83, 2019, doi: 10.1016/j.ijfatigue.2018.12.029.
[9] S. Kleszczynski and A. Elspaß, "Influence of isolated structural defects on the static mechanical properties of PBF-LB/M components," *Procedia CIRP*, vol. 94, pp. 188–193, 2020, doi: 10.1016/j.procir.2020.09.036.
[10] A. Martucci, A. Aversa, and M. Lombardi, "Ongoing Challenges of Laser-Based Powder Bed Fusion Processing of Al Alloys and Potential Solutions from the Literature-A Review," *Materials*, vol. 16, no. 3, 2023, doi: 10.3390/ma16031084.
[11] Yukitaka Murakami, Toshio Takagi, Kentaro Wada, and Hisao Matsunaga, "Essential structure of S - N curve: Prediction of fatigue life and fatigue limit of defective materials and nature of scatter,"
[12] A. Du Plessis, I. Yadroitsava, and I. Yadroitsev, "Effects of defects on mechanical properties in metal additive manufacturing: A review focusing on X-ray tomography insights," *Materials & Design*, vol. 187, p. 108385, 2020, doi: 10.1016/j.matdes.2019.108385.
[13] H. Gong, K. Rafi, T. Starr, and B. Stucker, "Effect of Defects on Fatigue Tests of As-Build Ti-6Al-4V Parts Fabricated by Selective Laser Melting," 2012.
[14] J. V. Gordon *et al.,* "Defect structure process maps for laser powder bed fusion additive manufacturing," *Additive Manufacturing*, vol. 36, p. 101552, 2020, doi: 10.1016/j.addma.2020.101552.
[15] H. Gong, K. Rafi, H. Gu, T. Starr, and B. Stucker, "Analysis of defect generation in Ti–6Al–4V parts made using powder bed fusion additive manufacturing processes," *Additive Manufacturing*, 1-4, pp. 87–98, 2014, doi: 10.1016/j.addma.2014.08.002.
[16] B. Zhang, Y. Li, and Q. Bai, "Defect Formation Mechanisms in Selective Laser Melting: A Review," *Chin. J. Mech. Eng.*, vol. 30, no. 3, pp. 515–527, 2017, doi: 10.1007/s10033-017-0121-5.
[17] C. Panwisawas, Y. T. Tang, and R. C. Reed, "Metal 3D printing as a disruptive technology for superalloys," *Nature communications*, vol. 11, no. 1, p. 2327, 2020, doi: 10.1038/s41467-020-16188-7.
[18] A. Ladewig, G. Schlick, M. Fisser, V. Schulze, and U. Glatzel, "Influence of the shielding gas flow on the removal of process by-products in the selective laser melting process," *Additive Manufacturing*, vol. 10, pp. 1–9, 2016, doi: 10.1016/j.addma.2016.01.004.

[19] R. Li, J. Liu, Y. Shi, L. Wang, and W. Jiang, “Balling behavior of stainless steel and nickel powder during selective laser melting process,” *Int J Adv Manuf Technol*, vol. 59, 9-12, pp. 1025–1035, 2012, doi: 10.1007/s00170-011-3566-1.
[20] S. Cao *et al.,* “Defect, Microstructure, and Mechanical Property of Ti-6Al-4V Alloy Fabricated by High-Power Selective Laser Melting,” *JOM*, vol. 69, no. 12, pp. 2684–2692, 2017, doi: 10.1007/s11837-017-2581-6.
[21] M. Grasso, A. Remani, A. Dickins, B. M. Colosimo, and R. K. Leach, “In-situ measurement and monitoring methods for metal powder bed fusion: an updated review,” *Meas. Sci. Technol.*, vol. 32, no. 11, p. 112001, 2021, doi: 10.1088/1361-6501/ac0b6b.
[22] L. R. Goossens and B. van Hooreweder, “A virtual sensing approach for monitoring melt-pool dimensions using high speed coaxial imaging during laser powder bed fusion of metals,” *Additive Manufacturing*, vol. 40, p. 101923, 2021, doi: 10.1016/j.addma.2021.101923.
[23] SLM Solutions GmbH, *SLM 280 Hl 1.0.* [Online]. Available: https://pdf.directindustry.com/pdf/slm-solutions/slm-280-hl/114591-626987.html (accessed: May 25 2023).
[24] PHOTRON USA, INC., *Photron GmbH NOVA S6-800K-M-16GB.* [Online]. Available: https://photron.com/de/fastcam-nova-s/ (accessed: Aug. 17 2023).
[25] I. Midwest Optical Systems, *MidOpt. SP785 Near-IR Dichroic Shortpass.* [Online]. Available: https://midopt.com/filters/sp785/ (accessed: Aug. 17 2023).
[26] Navitar Inc, *Navitar Inc. 12X Distanz Makro Zoom.* [Online]. Available: https://navitar.com/products/imaging-optics/high-magnification-imaging/12x-zoom/ (accessed: Apr. 17 2023).
[27] Edmund Optics Inc., *Protected Silver, λ/20 Mirror.* [Online]. Available: https://www.edmundoptics.eu/p/15mm-dia-protected-silver-lambda20-mirror/3761/ (accessed: May 25 2023).
[28] L. Crovini and L. Galgani, “On the accuracy of the experimental proof of Planck’s radiation law,” *Lett. Nuovo Cimento*, vol. 39, no. 10, pp. 210–214, 1984, doi: 10.1007/bf02783673.
[29] M. Planck, “Zur Theorie des Gesetzes der Energieverteilung im Normalspectrum,” *Phys. Bl.*, vol. 4, no. 4, pp. 146–151, 1948, doi: 10.1002/phbl.19480040404.
[30] P. von Böckh and T. Wetzel, “Strahlung,” in *Wärmeübertragung*, P. von Böckh and T. Wetzel, Eds., Berlin, Heidelberg: Springer Berlin Heidelberg, 2011, pp. 191–215.
[31] (. EOS, *Material Datasheet eos stainlesssteel 316l.* [Online]. Available: https://www.eos.info/
[32] J. Metelkova, Y. Kinds, K. Kempen, C. de Formanoir, A. Witvrouw, and B. van Hooreweder, “On the influence of laser defocusing in Selective Laser Melting of 316L,” *Additive Manufacturing*, vol. 23, pp. 161–169, 2018, doi: 10.1016/j.addma.2018.08.006.
[33] D. Turnbull, “Formation of Crystal Nuclei in Liquid Metals,” *Journal of Applied Physics*, vol. 21, no. 10, pp. 1022–1028, 1950, doi: 10.1063/1.1699435.
[34] D. H. StJohn, A. Prasad, M. A. Easton, and M. Qian, “The Contribution of Constitutional Supercooling to Nucleation and Grain Formation,” *Metall Mater Trans A*, vol. 46, no. 11, pp. 4868–4885, 2015, doi: 10.1007/s11661-015-2960-y.
[35] N. Schnell, M. P. Ferreira, J. Wegner, W. Tillmann, and S. Kleszczynski, “Process strategy for crack-free production of diamond-reinforced metal matrix composites with minimal graphitization through laser powder bed fusion,” *Diamond and Related Materials*, vol. 135, p. 109788, 2023, doi: 10.1016/j.diamond.2023.109788.
[36] N. Schnell, J. Wegner, A. Elspaß, and S. Kleszczynski, “Effective absorptivity of diamond-reinforced metal matrix composites for powder bed fusion using a laser beam,” *Additive Manufacturing Letters*, vol. 6, p. 100138, 2023, doi: 10.1016/j.addlet.2023.100138.

[37] M. Frey *et al.,* “Laser powder bed fusion of Cu-Ti-Zr-Ni bulk metallic glasses in the Vit101 alloy system,” *Additive Manufacturing*, vol. 66, p. 103467, 2023, doi: 10.1016/j.addma.2023.103467.
[38] J. Wegner, J. P. Best, N. Schnell, and S. Kleszczynski, “Structural deviations of bulk metallic glasses in downfacing surfaces fabricated via Laser Powder Bed Fusion,” *Procedia CIRP*, vol. 111, pp. 105–110, 2022, doi: 10.1016/j.procir.2022.08.147.
[39] B. Lane *et al.,* “Measurements of melt pool geometry and cooling rates of individual laser traces on IN625 bare plates,” *Integrating materials and manufacturing innovation*, vol. 9, no. 1, 2020, doi: 10.1007/s40192-020-00169-1.